

## Microstructure collapse: A shortcut to skip lengthy cyclic voltammetric activation in oxygen evolution reaction

Hao Ze Zheng<sup>a</sup>, Xiao Hu Wang<sup>a</sup>, Qiang Zeng<sup>a</sup>, Ze Zhuan Jiang<sup>b</sup>, Cheng Jiang<sup>a</sup>, Jun Sen Pang<sup>a</sup>, Wei Wei Yu<sup>a</sup>, Yan Shi<sup>a</sup>, Hong Qun Luo<sup>a,\*</sup>, Nian Bing Li<sup>a,\*</sup>

<sup>a</sup> School of Chemistry and Chemical Engineering, Southwest University, Chongqing 400715, PR China

<sup>b</sup> School of Materials and Energy, Southwest University, Chongqing 400715, PR China



### ARTICLE INFO

#### Keywords:

Microstructure collapse  
Oxygen evolution reaction  
Prussian blue analogue  
Thiophosphates  
Ternary

### ABSTRACT

This work outlines a simple yet ingenious approach to enhance performance of catalysts and stabilization in oxygen evolution reaction (OER) by rapidly disrupting microstructure. Prussian blue analogue (PBA) nanospheres (NS), designed as advanced electrocatalysts, are based on  $\text{Ni}_3\text{S}_2@\text{FeCoNi}$  and phosphorization. Thermal oxidation can allow NS to undergo microstructural collapse and form nanorubble (NR). NR obtained at 325 °C has a lower overpotential (230.0 mV) than NS. The material reaches its optimum condition directly, skipping tedious cyclic voltammetric (CV) activation. Collapse has regular properties, which are evidenced in some materials. No significant performance degradation during 1000 h ( $j = 10 \text{ mA cm}^{-2}$ ) and 24 h ( $j = 500 \text{ mA cm}^{-2}$ ) of electrolysis confirms excellence of this unconventional pathway. Theoretical calculations show the exposure of amorphous state from collapse enriches charges on the material surface, which helps to promote transformation of intermediates at the catalytic microinterfaces and accelerates the reaction process.

### 1. Introduction

Hydrogen represents a vital, sustainable energy resource in the ongoing campaign to address pressing environmental challenges and insufficient supply of fossil fuels [1–5]. Electrochemical water decomposition for hydrogen production is increasingly prevalent across a range of methods [6–8]. Typically, water electrolysis is comprised of two distinct half-reactions: an anodic reaction for oxygen evolution reaction (OER) and hydrogen evolution reaction (HER) [9,10]. Among others, the OER process involves the transfer of multiple protons and electrons, resulting in slow kinetics in the hydrolysis dissociation process compared to the HER half-reaction. Therefore, the high overpotential required to drive the OER reaction severely limits the energy efficiency of water electrolysis [11–15]. Although catalysts based on the noble metals  $\text{IrO}_2$  and  $\text{RuO}_2$  are commercially available, the scarcity and high cost of the materials, determined by elemental abundance, make the implementation of large-scale efficient noble metal-based OER processes very challenging. Therefore, the goal of contemporary researchers is to create and optimize non-precious metal catalysts with high catalytic activity, which is an effective cost reduction strategy for electrolysis of water. However, the catalysts generally undergo a long activation

process before being put into use, which increases the cost of the catalysts in disguise [16–18].

Prussian blue analogue (PBA) is a representative coordination polymer material consisting mainly of a metal ion center and a cyanide ligand [19–21]. The general formula for the material is  $\text{A}_x\text{B}[\text{M}(\text{CN})_6]_y \cdot \text{nH}_2\text{O}$ , where A represents alkali metals like Li, Na, and K; B and M represent transition metals such as Ni, Fe, Co, Zn, Mn, etc., [22–24]. The various transition metal ions in PBA provide the material with tunable metal active sites. Its open framework structure is an inherent property that enables derived materials such as alloys and phosphides to have uniform active sites and large specific surface areas. This makes it a widely used material in electrocatalytic water splitting [25–28]. Currently, the reported strategies for the synthesis of PBAs mainly include co-precipitation and etching. Notably, PBAs precursors synthesized by direct etching of metals or metal hydroxides via  $\text{K}_3[\text{M}(\text{CN})_6]$  (M = Ni, Co, Fe) have been extensively studied [29,30]. Unfortunately, most reported PBA-derived nanomaterials focus on a single anionic bimetallic heterostructure, which limits their electrocatalytic performance and electrical conductivity [31–34].

In this work, iron, cobalt and nickel were used to construct a ternary PBA.  $\text{Ni}_3\text{S}_2$  nanosheets were used as a self-sacrificing template in the

\* Corresponding authors.

E-mail addresses: luohq@swu.edu.cn (H.Q. Luo), linb@swu.edu.cn (N.B. Li).

interfacial redox reaction. A carefully designed double-negative-triple-anodic heterostructure ( $\text{Ni}_3\text{S}_2@\text{Fe}-\text{Co}-\text{Ni}_2\text{P}$ ) after thermal phosphating treatment shows a special nanosphere (NS) structure created by fusing nanocubes. Thermal oxidation was employed to induce the collapse of NS, destroying its original structure and morphology. This led to the exposure of more active sites of the catalyst, effectively increasing its efficacy and reaching the activated state of the catalyst earlier. Detailed electrochemical analyses confirmed the excellent OER electrocatalytic activity of the collapsed material. At a current density of  $10 \text{ mA cm}^{-2}$ , NS in 1.0 M KOH required an overpotential of 252.5 mV and a CV activation time of 12 h, whereas the nanorubble (NR) obtained at 325 °C (325-NR) required an overpotential of only 230.0 mV and a reconstruction time of 2 h without CV activation at the same current density. In addition, the 325-NR can be operated for 1000 h without significant degradation in performance. At a current density of  $500 \text{ mA cm}^{-2}$ , the 325-NR can achieve a low overpotential of 676 mV and maintain excellent stability for 24 h. The material shows potential for use as an industrial catalyst due to its low cost and high efficiency, making it a viable candidate. Theoretical calculations show that the presence of amorphous metal oxides redistributes the charge and tends to enrich it on the surface of the material, improving the OER performance of 325-NR [9,35].

## 2. Experimental section

### 2.1. Materials

Thiourea was obtained from Titan General-reagent (Shanghai, China). Hydrochloric acid (HCl, 37 wt%) was purchased from Kelong Chemical Reagent Factory (Chengdu, China). All other drugs were purchased from Titan Adama-betas (Shanghai, China). Ni foam was purchased from Ce Tech Co., Ltd. (Taiwan, China). All chemicals were used as received without further purification. Deionized water ( $18.2 \text{ M}\Omega \text{ cm}$ ) was used throughout the experiments.

### 2.2. Synthesis

#### 2.2.1. Synthesis of precursor for nickel sulfide nanosheets

A piece of foam nickel ( $2 \text{ cm} \times 3 \text{ cm}$ ) was put into 3.0 M HCl for ultrasound for 15 min. And then it was taken out and washed with water and ethanol alternately. The nickel foam was dried in a 60 °C oven for 6 h and then it was placed in a 50 ml polytetrafluoroethylene lining for later use. 0.5 mmol of thiourea, 2.0 mmol of ammonium fluoride, and 1.0 mmol of nickel nitrate hexahydrate were dissolved in 20 ml of water. The mixture was stirred for 30 min until completely dissolved and then poured into the aforementioned polytetrafluoroethylene, which placed in an oven and kept at 120 °C for 10 h. After heating, it was quickly taken out for cooling. The foam nickel was taken out when it returns to room temperature. It was washed with deionized water and ethanol for three times alternately, dried in an oven at 60 °C for 12 h and marked as a precursor.

#### 2.2.2. Synthesis of ternary PBA

The dried precursor was placed in a polytetrafluoroethylene lining for future use. 0.2 mmol of potassium ferrocyanide is dissolved in 10 ml of water, stirred until completely dissolved, and labeled as liquid A. 0.2 mmol of cobalt (II) cyanide potassium was directly added to solution A. After stirring until completely dissolved, 10 ml of deionized water was added. All the above solutions were transferred to the PTFE lining. After assembling the high-pressure reactor, it was placed in an oven and held at 90 °C for different times. After heating, the material was taken out and dried in a 60 °C oven for 12 h to obtain different forms of X-PBA (X represents hydrothermal time).

#### 2.2.3. Synthesis of nanospheres

PBA was placed downstream of the tubular furnace, and 1.0 g of

anhydrous sodium hypophosphite was taken out and placed in the magnetic boat upstream of the tubular furnace. The temperature was raised from room temperature to 350 °C at a rate of  $1 \text{ }^{\circ}\text{C min}^{-1}$  and maintained for 2 h. After the room temperature was restored, the materials were taken out and obtained the nanosphere.

#### 2.2.4. Construction of nanorubble

The NS mentioned above was placed in a magnetic boat, and the temperature of the furnace was raised to the target temperature in advance. When the temperature was stable, the porcelain boat was directly pushed into the inner chamber, kept for 1 h, and then freely cooled to obtain a collapsed shaped material. The sample obtained is denoted as T-NR (T is the temperature of collapse).

## 2.3. Characterization

XRD patterns of the products were tested with an X-ray diffractometer (Purkinje General Instrument XD-6) by Cu K $\alpha$  radiation ( $\lambda = 1.5406 \text{ nm}$ ). The scanning range is 5–90°. The scanning rate is  $2 \text{ }^{\circ}\text{ min}^{-1}$ . The morphologies and element composition were sequentially investigated by a field-emission scanning electron microscopy (FESEM, S4800, Hitachi, Japan), energy-dispersive X-ray spectroscopy (EDX, GENESIS, EDAX, USA), and transmission electron microscope (TEM, Tecnai G220, Fei Corporation, Japan). The chemical states of the samples were analyzed with X-ray photoelectron spectroscopy (XPS, Thermo ESCALAB 250Xi, Thermoelectricity Instruments, USA) surface analysis system. The white light interferometer is the Atometrics-EX230. Sulphur vacancies were analyzed by electron paramagnetic resonance (EPR, Bruker ELEXSYS-II E500, Germany).

## 2.4. Electrochemical measurements

All electrochemical measurements were performed using a CHI Electrochemical Workstation (Model 660E) in a 1.0 M KOH solution. A three-electrode system at room temperature was used, where nickel foam (NF) with the catalysts was used directly as the working electrode ( $0.5 \text{ cm}^2$  electrode area), and Hg/HgO and graphite rod were used as the reference electrode and counter electrode, respectively. Polarization curves were recorded by linear sweep voltammetry (LSV) at a scan rate of  $5 \text{ mV s}^{-1}$ . The Tafel slopes were derived from a linear fit utilizing the Tafel equation ( $\eta = b \log j + a$ , where  $\eta$  is the overpotential,  $b$  is the Tafel slope,  $j$  is the current density, and  $a$  is the adjusted constant). Electrochemical impedance spectroscopy (EIS) measurements were performed at the different overpotentials with a perturbation of 5 mV amplitude in the range from 10 kHz to 0.01 Hz.

## 2.5. In-situ Raman spectra measurements

Raman spectra were acquired on a Renishaw inVia reflex Raman microscope under an excitation of 633 nm. A three-electrode system was used for in-situ Raman spectra measurement with NS/325-NR as a working electrode, a Pt wire as the counting electrode, and an Ag/AgCl electrode as the reference electrode. All electrodes were placed in a Teflon electrochemical cell with the examined sample at the top facing to the objective lens. The electrolyte used was 1.0 M KOH. To monitor the evolution of catalyst samples during the OER process, the Raman spectra were immediately collected after a 200, 400, 600, 800, and 1000 s with a scan rate of  $1 \text{ mV s}^{-1}$  from 0.9 to 1.9 V by using an electrochemical work station. Scanning was paused while Raman spectra were collected.

## 3. Results and discussion

Here we identify the "Nanorubble" as an integrated structure on the catalyst surface that undergoes a series of collapses and reconstructions. In this study, this structure is induced by thermal oxidation, which can

lead to the tendency of the material to form a natural stable state in thermal environments based on its own properties. Structures remodelled by heat treatment show superior stability and we have exploited the remodelling induced by this transformation to further optimize the properties. Unlike conventional experiments involving self-evolutionary-induced surface remodeling, this method allows the material to bypass the long-waiting activation process described above, rapidly reaching a surface stable state and fully stimulating its OER potential (Fig. 1a). After the same CV process, NR did not undergo significant performance changes. Although NS showed improved performance after a long CV, NR performed significantly better (Fig. 1b). NS can slowly reach the optimal state it can reach by means of CV during the 12 h activation process (Fig. S1), whereas no significant performance change of NR was observed during CV because it reaches its final state earlier (Fig. S2). Moreover, NS before and after CV activation exhibited significant morphological changes (Figs. 1c and 1d), while NR did not observe significant morphological changes before and after undergoing CV treatment (Figs. 1e and 1f). Underneath this seemingly homogeneous profile are different formation mechanisms, which lead to significant differences in the level of performance optimization. Here we observe and exploit the faster path of such performance optimization and investigate the mechanism of action in detail.

### 3.1. The shaping process and characterization of NR

Constructing a full framework is akin to constructing a building, where designated materials are necessary for the foundation, structural support, and functional components. In this study,  $\text{Ni}_3\text{S}_2$  acts as a base material due to its excellent metallic properties and electrical conductivity, and in particular as a high performance substrate due to its hierarchical layered structure (Fig. S3). At the same time, the cyano-coordination compounds serve as structural carriers. Fe, Co, and Ni operate as functional components in delivering the different reaction sites [36]. The development from  $\text{Ni}_3\text{S}_2$  to PBA has produced nanocubes composed of cyano-coordinated compounds that embody a homogeneous rectangular structure (Fig. S4). The catalytic effect of FeCoNi PBA varied depending on the duration of the hydrothermal heat, with the best performance observed at 6 h (Fig. S5a). In addition, analyses by double layer capacitance ( $C_{dl}$ ) (Fig. S5b), Tafel slope (Fig. S5c), EIS (Fig. S5d), and CV (Fig. S6) demonstrated the extraordinary effectiveness of the 6 h PBA, prompting the selection for further studies. The PBA nanocubes were phosphated to enhance their electrocatalytic properties by transforming the stable square structure into nanospheres with

improved electron conductivity. The optimal phosphating time was found to be 2 h (Fig. S7). Depending on the applied temperature, thermal oxidation was utilized to induce the collapse of NSs into varying levels of collapse (Fig. S8). The formation of stable multi-interstitial rubble structures by moderate thermal oxidation leads to increased exposure of active material components, which enhances the stability.

The initial ternary PBAs exhibited a square structure, which limited the exposure of active sites and electron transfer capability due to the dense stacked layers. The excessive thickness of this structure subsequently led to insufficient conductivity and electrocatalytic activity [11, 13]. In addition, the accumulation of dross has a negative effect on the performance of PBA. Phosphating treatment changed the structure of PBA and enhanced its stability and catalytic activity.

Although some improvements were made, NS did not reach the desired level of stability and activity. Analysis of the microstructural collapse showed a substantial increase in stability and structural rearrangement due to thermal oxidation-induced collapse of NS. This resulted in the development of a porous and robust structure that was immune to external influences. Several analytical techniques were used to study the extent of collapse in NS, namely SEM, XRD, TEM, XPS and white light interference. The temperature was varied to obtain observations on the morphological and chemical changes that occurred. As shown in Fig. 2a-d, the NS begins to transition from nanospheres to planes as the extent of collapse increases. It is like the process of a building being hit by an earthquake and turning into rubble (Fig. 2e). Skeletal fragments generated as a result of collapse can be observed (Fig. S9). White light diffraction was used to measure the change in catalyst surface roughness at different collapse temperatures (Figs. 2f and S10). Models were built to show the characteristics of each morphology more graphically based on the features of the material at each temperature (Figs. 2g and S11). It was observed that the higher the temperature, the smoother the surface. XRD confirmed the disappearance of the characteristic PBA peaks after phosphatization (Fig. 2h). XRD tests were performed on the NR (Fig. 3a). A broad peak belonging to C appeared at  $20^\circ - 30^\circ$ , and C originated from the cyano skeleton exposed after collapse. TEM images identified the surface materials of 325-NR as  $(\text{Fe}, \text{Ni})_2\text{P}$  and  $\text{Ni}_2\text{P}$  (Figs. 3b, 3c, and 3d). Fig. 3e shows the full XPS spectra of different catalysts. The continuous collapse of the microstructure makes the corresponding XPS spectra of each element show different variations as well. The most obvious is S. As the microstructure collapse deepens, S can be detected in  $\text{Ni}_3\text{S}_2$  again (Fig. 3f). The deepening of the collapse can also be seen in the peak of Ni (Fig. 3g). The twin peaks at 786.64/806.40 eV are considered to be satellite peaks.

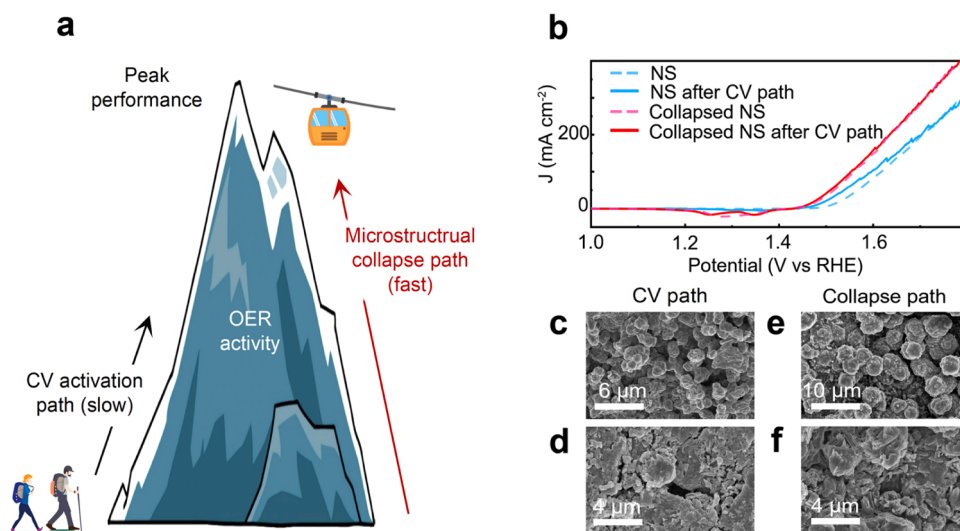


**Fig. 1.** (a) Schematic illustration of different OER activation paths of NS. (b) LSV curves of NS and NR before and after CV activation. SEM images of (c) NS, (d) NS after CV path, (e) NR and (f) NR after CV path.

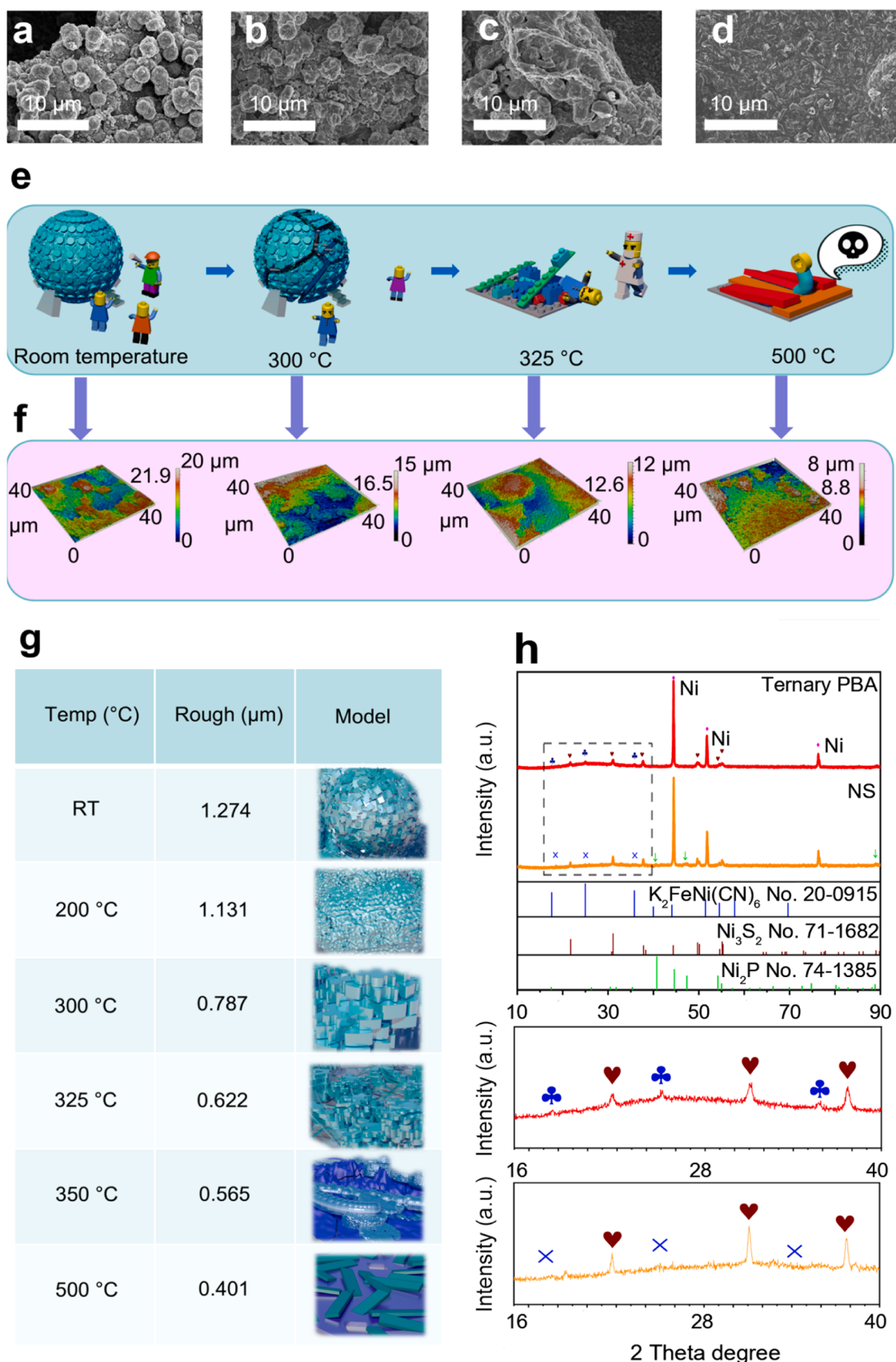


**Fig. 2.** SEM images of (a) room temperature-NS, (b) 300-NR, (c) 325-NR, and (d) 500-NR. (e) Toy models with varying shapes. (f) White light interference of materials with different levels of collapse. (g) Roughness and partial models. (h) XRD images of PBA and NS.

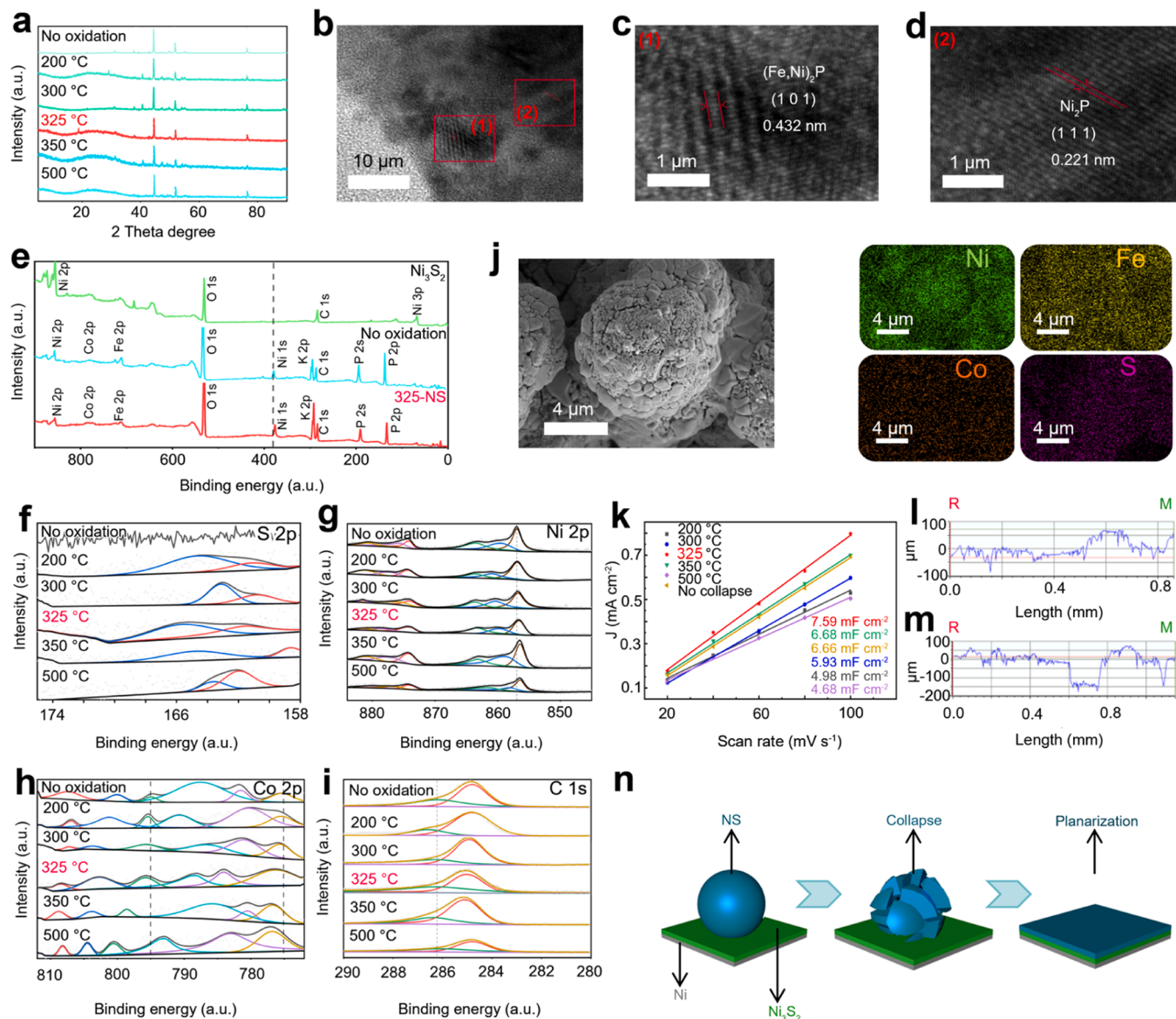


**Fig. 3.** (a) XRD image of NR at different temperatures. (b) TEM image of 325-NR. (c), (d) are partially enlarged images of (b). (e) XPS full spectrum of different catalysts. The XPS images of (f) S 2p, (g) Ni 2p, (h) Co 2p and (i) C 1s of NS and NR. (j) EDX images of 325-NR. (k) The calculated electrochemical double-layer capacitance of NR at different temperatures. Outline of (l) NS and (m) 325-NR. (n) Diagram of the planarization process.

Ni 2p in the material was deconvoluted into three binary states. 856.33/873.85 eV is the phase combining Ni<sup>δ+</sup> and P bonds. 857.96/875.75 eV is the Ni<sup>2+</sup> phase, while 863.05/880.33 eV is the satellite peak. Thermal oxidation gives the material surface a metallic oxidation state. Interestingly, the 2p peak of Ni gradually shifted towards lower binding energy as the collapse level increased, implying a gradual increase in the amount of low-valent Ni on the surface of the material. This is attributed to the carbon in the cyano skeleton of the material reducing the high-valent Ni. The two peaks bound to Co<sup>2+</sup> and P are shifted towards higher binding energies (Fig. 3h), due to the oxidation of Co at increasingly higher temperatures of microstructural collapse. The carbon in the skeleton is difficult to stabilize at higher temperatures and would allow for a more complete reduction of Ni. Co is oxidized while Ni is reduced, attributed to the difference in their contents. Small amounts of Co have a lower probability of being reduced by carbon than Ni. This is also evidenced by the full spectrum: the Ni 1 s peak of the material collapsing at 325 °C is slightly shifted towards lower binding energies compared to the material not collapsed, demonstrating the formation of low-valent Ni in the process. For the XPS of C (Fig. 3i), the peak

originally located at 286.4 eV is shifted towards higher binding energies. This indicates a gradual increase in the C oxidation state. Secondly, the proportionality between the two peaks of C1s was analyzed. The level of material collapse (blue peaks/red peaks) was indirectly confirmed using the ratio of peak areas. The ratio called the carbon ratio. As the level of collapse increases, the carbon ratio decreases and approaches zero. This indicates that more and more low valence carbon is produced at the surface of the material. The decrease in the carbon ratio is evidence of successful construction of the collapse, which leads to large-scale exposure of carbon in the skeleton. XPS of Fe can be fitted to four peaks (Fig. S12). The peak at 709.24/723.18 eV belongs to Fe<sup>2+</sup>, the peak at 713.70 eV belongs to Fe<sup>3+</sup>. The wave at 710.76 eV belongs to an oscillating satellite peak. Although the content of Fe is more than that of Co, it is still much lower than that of Ni, so the peak also shows a higher binding energy shift, reflecting the deepening of the oxidation. The XPS of P was demonstrated as a single peak. The amount of sodium hypophosphite added during the phosphatization process was sufficiently large for a single phosphate valence to appear on the surface of the material (Fig. S13). To summarize the process: thermal oxidation leads

to the collapse of NS, exposing the cyano skeleton and  $\text{Ni}_3\text{S}_2$  at the bottom. This leads to an increase in the surface C content of the material and the reproduction of S. The surface C content of the material is then increased by the addition of sodium hypophosphite. NS consists mainly of Ni, with small amounts of Fe and Co having a significantly greater oxidizing effect than Ni. Note that "small amounts" here is relative to Ni. The uniform distribution of the elements was demonstrated using high-angle annular dark-field scanning transmission electron microscopy (STEM-EDX) images (Figs. 3j, S14, and S15), and electrochemical double-layer capacitance calculations of NS at different temperatures (Fig. 3k and S16) further demonstrated the change in electrochemically active area after microstructure collapse. 325-NR has the largest electrochemically active area. To further understand the intrinsic activity of each active site, we performed electrochemically active surface area (ECSA) normalization. The corresponding ECSA were calculated as shown in Table S1. As we expected, the normalized curves demonstrate that the ECSA-normalized current density ( $J_{\text{ECSA}}$ ) of 325-NR is smaller

than that of the other samples (Fig. S17), proving that different microstructural collapses carried out on the same material result in different specific surface area changes. Contour tests were performed on the edges of NS (Fig. 3l). This material collapsed into NR at 325 °C and was again contoured (Fig. 3m). It is clear that NS underwent microstructural collapse. Based on the above tests, we can basically determine that the collapse process consists of three main steps: formation-collapse-planarization (Fig. 3n). The results obtained confirm the phenomenon of morphological collapse. Valuable insights into the collapse process were gained through these analytical techniques, particularly with regard to the formation, covering and remodeling of collapsed structures.

### 3.2. Implications of microstructure collapse for performance enhancement

The proposed microstructure collapse method for electrocatalysis offers several significant advantages. Moreover, the effectiveness of the method has been demonstrated in several studies highlighting its

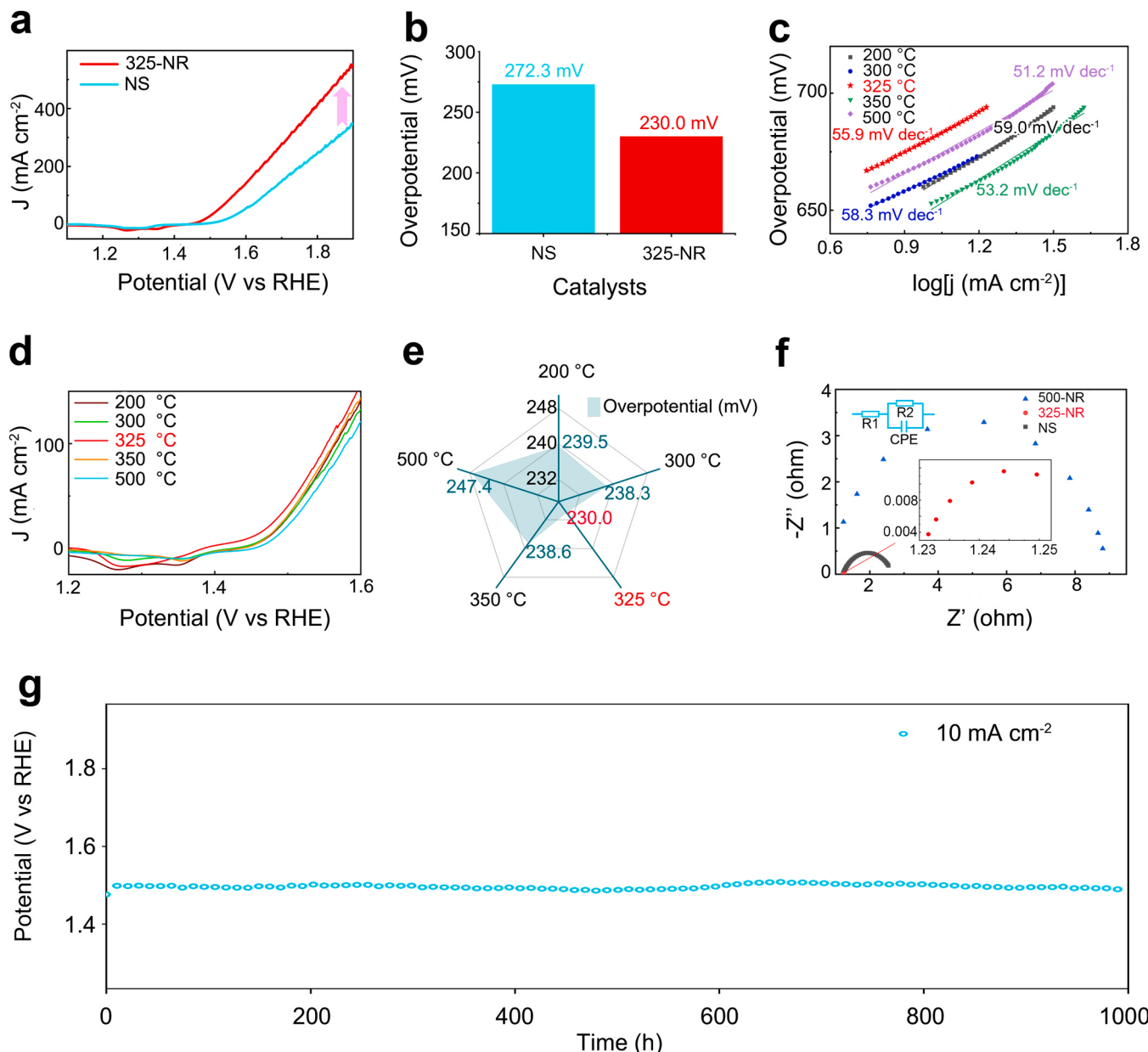


**Fig. 4.** (a) Comparison of LSV curves before and after microstructure collapse. (b) Bar chart of NS and 325-NR. (c) Tafel curves and (d) LSV curves of NR at different temperatures. (e) Radar chart of NR overpotential at different temperatures. (f) EIS curves of NS and NR at different temperatures. Inset (the upper left corner) is the corresponding equivalent circuit model. (g) Stability test of 325-NR.

potential to significantly improve electrocatalytic performance. Firstly, the method for triggering microstructure collapse is not complicated. It only requires the use of simple physical or chemical methods, such as a rapid increase in temperature or pressure. This simplicity is easy to implement as it does not require complex procedures or the addition of different reagents. Second, regulating the level of collapse is simple. Different gradient temperatures can effectively control the collapse, which is easy to achieve. Finally, the time required for microstructure collapse is short. The use of intensive physical or chemical methods to build the collapsed structure ensures rapid completion, resulting in significant time and cost savings. For comparison, we investigated the OER catalytic performance of NS, 325-NR, and other catalysts (Fig. S18). We observed that the performance of NS was significantly enhanced after the introduction of microstructure collapse. It is worth mentioning that 325-NR and commercial  $\text{IrO}_2$  have similar overpotentials at a current density of  $10 \text{ mA cm}^{-2}$ . However, at high current densities, 325-NR performs much better than commercial  $\text{IrO}_2$ . The overpotential of 325-NR was reduced by 42.3 mV compared to NS (Figs. 4a and 4b). In addition, we investigated the Tafel slopes of NR with different microstructural collapses (Fig. 4c). The Tafel slope of 325-NR is not the lowest because the electron transfer rate depends on the cohesive force between the various components. The greater the level of collapse, the more fragmented microstructures adhere to the substrate, thus increasing the electron transfer rate. We also evaluated the OER catalytic activity of NRs with different levels of disintegration (Fig. 4d). The fluctuations on current density in the range of 1.2–1.3 V were attributed to the reduction peaks of the metal oxides caused by the reverse scan we performed. 325-NR exhibited the smallest overpotential, 230.0 mV (Fig. 4e). With increasing temperature, the overpotential decreases before increasing. EIS showed that 325-NR had the lowest resistance ( $R_{ct}$ ) (Fig. 4f), indicating rapid electron transfer between the catalyst and electrolyte. The stability of 325-NR was evaluated at a current density of  $10 \text{ mA cm}^{-2}$  (Fig. 4g). The results showed that 325-NR exhibited continuous electrolysis for 1000 h without exhibiting any significant performance degradation. We performed SEM (Fig. S19), TEM (Fig. S20), XRD (Fig. S21), and XPS (Fig. S22) on 325-NR after 1000 h stability test. The results proved that there was no significant change in the 325-NR after a long stability test. Furthermore, in order to investigate the potential for industrialization of 325-NR, stability tests were performed at a current density of  $500 \text{ mA cm}^{-2}$  (Fig. S23). The data suggest that microstructure collapse has a practical and positive effect on improving the OER performance of the catalyst. The electrocatalytic performance of 325-NR is superior among the samples tested. In addition to the good stability of 325-NR, the overpotentials were found to be relatively small compared with some electrocatalysts in the OER field (Table S2).

In-situ Raman spectroscopy was used to further illustrate that microstructure collapse is the main reason for the enhanced catalyst performance. We tested the in-situ Raman spectra of NS and 325-NR, respectively (Fig. S24). For NS, the peaks located at 479 and  $560 \text{ cm}^{-1}$  both belong to  $\text{Ni}^{3+}\text{-O}$ . During the OER process, these two peaks become higher with a large level of variation. This proves that NS undergoes a very obvious surface remodelling during the OER process. Compared to NS, these two peaks of 325-NR underwent a slight blue shift, but the peak area did not show any significant change during the OER process. This strongly suggests that the remodelling that occurs on the catalyst surface after microstructure collapse is quite limited.

Encouraged by the excellent OER performance and stability of 325-NR, we assembled NS and 325-NR into alkaline overall water spilling electrolyzers, respectively. The electrolyzer assembled from 325-NR exhibited smaller overpotentials to deliver current densities of 10 and  $50 \text{ mA cm}^{-2}$  at 1.56 and 1.93 V (Fig. S25), respectively, which were superior to the NS electrolyzer.

### 3.3. An exploration of the theoretical genesis and pervasiveness of NR

In order to provide a theoretical explanation for the enhanced OER

catalytic activity of 325-NR after the introduction of collapse, we constructed computational models based on XRD (Fig. 3a) and ICP for NS and 325-NR (see Fig. S26 for construction details) and performed calculations on the equivalent surfaces of the charge density difference (Figs. 5a and 5b). The yellow area represents the electron gain region and the blue area represents the electron loss region. Comparisons show that the introduction of collapse leads to a strong electron redistribution significantly observed on the material surface. There is low charge aggregation on the NS surface (Fig. 5a). In contrast, there is a large charge accumulation in the interfacial region of 325-NR, indicating that this interfacial interaction leads to a strong electron redistribution (Fig. 5b). The electron localization function (ELF) further demonstrates the charge distribution on the surface of the material before and after microstructure collapse. The electrons of NS tend to bond inside the material with a small electron-rich region (Fig. 5c), and the bonding of 325-NR tends to be distributed in the outer layer of the material (Fig. 5d), which facilitates the transport of electrons during the reaction process and improves the efficiency of OER. Several cross sections were selected to reduce the fortuity, and the tendency of electrons to cluster on the outside of 325-NR is greater than that of the NS (Fig. S27). In order to demonstrate more comprehensively the effect of microstructure collapse on the OER process, the main reaction steps on the catalyst surface were investigated using DFT calculations (Figs. 5e and 5f). In combination with Bader charge analysis (Fig. 5g), electron gains and losses were quantified. The Bader charge for Co increases from  $-0.08\text{--}0.97$  (NS to 325-NR), while the charge number for Ni increases from  $-0.19\text{--}0.70$ , indicating a change from electron enrichment to electron depletion in both the Co and Ni regions. Notably, for Fe, the shift from 0.02 to 1.22 indicates a more drastic electron depletion. Thus, although the charge density difference indicates a charge transfer from the inside to the outside of the material, the Co and Fe regions change more than the Ni region, which fits well with the XPS results shown in Figs. 3g, 3h and S12. The above results do prove the strong electronic interactions at the interface. Fig. 5h shows the energy differences diagram of the main reaction pathway for alkaline OER. The free energy diagrams show that the rate-limiting step is the formation step from  $\text{O}^*$  to  $\text{OOH}^*$ , which can be achieved by 325-NR with only 1.76 eV. The results of TEM (Fig. S28a), XRD (Fig. S28b), and EDX (Fig. 3j) analyses show that the amorphous structure exhibits a highly homogeneous mixing. A reaction site was randomly selected on 325-NR (Fig. 5f). Randomly selected sites 1, 2, and 3 of NS were calculated (Figs. S29, S30, and S31), which require 2.93, 0.77, and 1.55 eV more energy than 325-NR, respectively, to achieve this step. It can be concluded that the amorphous mixed metal oxides resulting from microstructure collapse lead to a charge redistribution in 325-NR that increases the density of surface charges, facilitates electron transfer, and considerably reduces the activation energy of the key step in the OER reaction process. In order to explore other possibilities for the active site, EPR was used to detect the creation of S vacancies during the collapse process (Fig. S32). Combined with the experimental results, it can be inferred that the disappearance/appearance of S vacancies does not occur during the microstructure collapse of 325-NR. Therefore, the active sites of 325-NR include but are not limited to the metal mixed oxides, and there are other minor active sites acting synergistically as well.

It is important to emphasize that in parallel with our investigation of the generality, we evaluated the OER performance of the catalysts. K<sup>+</sup>-doped  $\text{Cu}_2\text{Se}$  nanopins with a one-dimensional structure showed the most superior catalytic performance at 180 °C (Figs. S33 and S34), whereas two-dimensional flaky NiFe-LDH had the best catalytic activity at 205 °C (Figs. S35 and S36). By integrating the 3D nanoparticles described in this paper, their best performance was achieved at 325 °C. The temperature required for microstructure collapse increases progressively as the material transitions from one to three dimensions. Because structures with higher dimensions are more stable and harder to destroy. This is consistent with our experimental phenomenon. The above process confirms the rationality of microstructure collapse and its

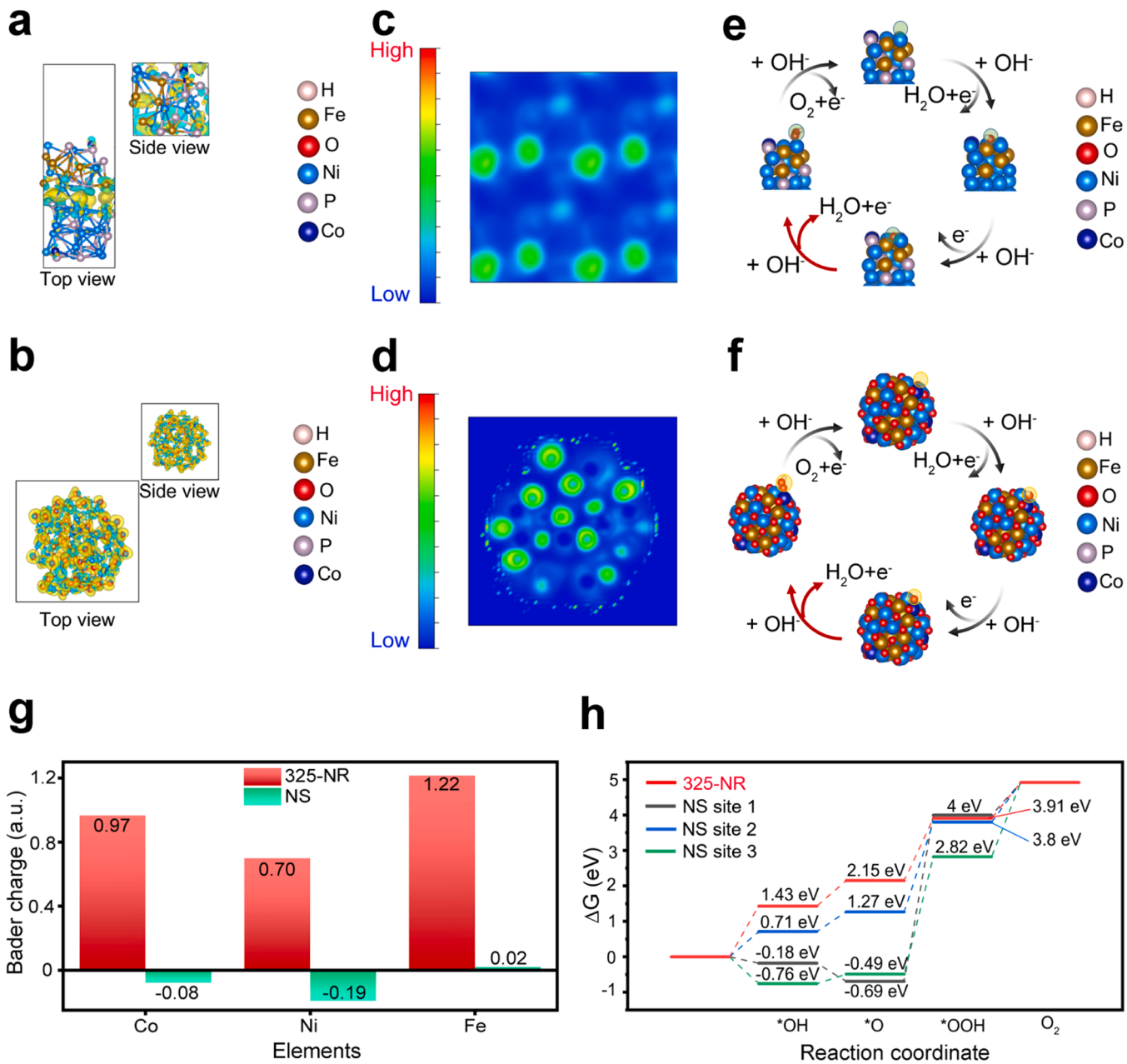


**Fig. 5.** (a) Charge distribution at the NS interface. (b) Charge distribution at the 325-NR interface. (c) ELF of NS. (d) ELF of 325-NR (High and low represent the level of electron enrichment). (e) DFT optimized NS site 1 structure. (f) DFT optimized 325-NR structure. (g) Average Bader charge of Fe, Co, Ni, in optimized supercell geometry for NS and 325-NR. (h) Free energy diagrams on NS and 325-NR.

general usefulness in OER catalyst design.

#### 4. Conclusion

In this work, a counterintuitive microstructure collapse method is proposed, along with an overview of the regularities and intrinsic properties of reverse-constructed catalysts. This method will skip the lengthy regular activation process of the catalyst and reach the catalyst optimum quickly and efficiently. Microstructure collapse will generate a very stable surface state *in situ*, thereby increasing the intrinsic and potential activity of the enabling material and greatly improving OER performance and stability. Compared to commercially available  $\text{IrO}_2$ , 325-NR offers significant advantages at high current densities. This will lay the foundation for high efficiency and large-scale production of industrialized catalysts. In addition, this method provides a new

reference point for researchers.

#### CRediT authorship contribution statement

**Hong Qun Luo:** Conceptualization, Methodology, Project administration, Resources, Writing – review & editing. **Nian Bing Li:** Conceptualization, Funding acquisition, Methodology, Project administration, Writing – review & editing. **Hao Ze Zheng:** Writing – original draft, Supervision, Software, Methodology, Investigation, Formal analysis, Conceptualization. **Xiao Hu Wang:** Software, Resources, Methodology, Data curation, Conceptualization. **Qiang Zeng:** Project administration, Methodology, Investigation, Formal analysis, Validation. **Ze Zhuan Jiang:** Supervision, Software, Resources, Methodology, Data curation. **Cheng Jiang:** Visualization, Software, Resources, Methodology, Data curation. **Jun Sen Pang:** Software, Methodology, Formal analysis, Data

curation. **Wei Wei Yu:** Conceptualization, Data curation, Software, Visualization. **Yan Shi:** Data curation, Formal analysis, Validation.

## Declaration of Competing Interest

The authors declare that they have no known competing financial interests or personal relationships that could have appeared to influence the work reported in this paper.

## Data availability

The data that support the findings of this study are available in the supplementary material of this article.

## Acknowledgements

This work was supported by the National Natural Science Foundation of China (No. 21675131), the Natural Science Foundation of Chongqing (No. cstc2020jcyj-zdxmX0003, No. CSTB2023NSCQMSX0924) and the Chongqing Returnee Overseas Students Entrepreneurship and Innovation Support Program (cx2022006).

## Appendix A. Supporting information

Supplementary data associated with this article can be found in the online version at [doi:10.1016/j.apcatb.2024.124029](https://doi.org/10.1016/j.apcatb.2024.124029).

## References

- [1] L.-M. Cao, D. Lu, D.-C. Zhong, T.-B. Lu, Prussian blue analogues and their derived nanomaterials for electrocatalytic water splitting, *Coord. Chem. Rev.* 407 (2020) 213156, <https://doi.org/10.1016/j.ccr.2019.213156>.
- [2] Y. Zeng, G.-F. Chen, Z. Jiang, L.-X. Ding, S. Wang, H. Wang, Confined heat treatment of a Prussian blue analogue for enhanced electrocatalytic oxygen evolution, *J. Mater. Chem. A* 6 (2018) 15942–15946, <https://doi.org/10.1039/C8TA05677C>.
- [3] X. Yang, L. Kang, Z. Wei, S. Lou, F. Lei, P. Hao, J. Xie, B. Tang, A self-sacrificial templated route to fabricate CuFe Prussian blue analogue/Cu(OH)<sub>2</sub> nanoarray as an efficient pre-catalyst for ultrastable bifunctional electro-oxidation, *Chem. Eng. J.* 422 (2021) 130139, <https://doi.org/10.1016/j.cej.2021.130139>.
- [4] X.H. Wang, Y. Ling, B. Wu, B.L. Li, X.L. Li, J.L. Lei, N.B. Li, H.Q. Luo, Doping modification, defects construction, and surface engineering: design of cost-effective high-performance electrocatalysts and their application in alkaline seawater splitting, *Nano Energy* 87 (2021) 106160, <https://doi.org/10.1016/j.nanoen.2021.106160>.
- [5] H. Zhang, Q. Jiang, J.H.L. Hadden, F. Xie, D.J. Riley, Pd ion-exchange and ammonia etching of a prussian blue analogue to produce a high-performance water-splitting catalyst, *Adv. Funct. Mater.* 31 (2021) 2008989, <https://doi.org/10.1002/adfm.202008989>.
- [6] X. Su, Y. Wang, J. Zhou, S. Gu, J. Li, S. Zhang, Operando spectroscopic identification of active sites in NiFe prussian blue analogues as electrocatalysts: activation of oxygen atoms for oxygen evolution reaction, *J. Am. Chem. Soc.* 140 (2018) 11286–11292, <https://doi.org/10.1021/jacs.8b05294>.
- [7] L. Quan, S. Li, Z. Zhao, J. Liu, Y. Ran, J. Cui, W. Lin, X. Yu, L. Wang, Y. Zhang, J. Ye, Hierarchically assembling CoFe prussian blue analogue nanocubes on CoP nanosheets as highly efficient electrocatalysts for overall water splitting, *Small Methods* 5 (2021) 2100125, <https://doi.org/10.1002/smtd.202100125>.
- [8] H. Zhang, J. Diao, M. Ouyang, H. Yadegari, M. Mao, M. Wang, G. Henkelman, F. Xie, D.J. Riley, Heterostructured core-shell Ni-Co@Fe-Co nanoboxes of prussian blue analogues for efficient electrocatalytic hydrogen evolution from alkaline seawater, *ACS Catal.* 13 (2023) 1349–1358, <https://doi.org/10.1021/acscatal.2c05433>.
- [9] H. Zhang, S. Geng, M. Ouyang, H. Yadegari, F. Xie, D.J. Riley, A self-reconstructed bifunctional electrocatalyst of pseudo-amorphous nickel carbide @ iron oxide network for seawater splitting, *Adv. Sci.* 9 (2022) e2200146, <https://doi.org/10.1002/advs.202200146>.
- [10] Q. Hu, Z. Wang, X. Huang, Y. Qin, H. Yang, X. Ren, Q. Zhang, J. Liu, C. He, A unique space confined strategy to construct defective metal oxides within porous nanofibers for electrocatalysis, *Energy Environ. Sci.* 13 (2020) 5097–5103, <https://doi.org/10.1039/D0EE02815K>.
- [11] A. Li, L. Zhang, F. Wang, L. Zhang, L. Li, H. Chen, Z. Wei, Rational design of porous Ni-Co-Fe ternary metal phosphides nanobricks as bifunctional electrocatalysts for efficient overall water splitting, *Appl. Catal. B Environ.* 310 (2022) 121353, <https://doi.org/10.1016/j.apcatb.2022.121353>.
- [12] X. Song, S. Song, D. Wang, H. Zhang, Prussian blue analogs and their derived nanomaterials for electrochemical energy storage and electrocatalysis, *Small Methods* 5 (2021) e2001000, <https://doi.org/10.1002/smtd.202001000>.
- [13] W.K. Gao, M. Yang, J.Q. Chi, et al., In situ construction of surface defects of carbon-doped ternary cobalt-nickel-iron phosphide nanocubes for efficient overall water splitting, *Sci. China Mater.* 62 (2019) 1285–1296, <https://doi.org/10.1007/s40843-019-9434-7>.
- [14] T. Li, Y. Yu, M. Pei, Dual-atom doping carbon materials as highly efficient electrocatalysts for lithium-sulfur batteries: bimetallic cooperation mechanism, *J. Phys. Chem. Lett.* 127 (2023) 6271–6279, <https://doi.org/10.1021/acs.jpcc.2c08262>.
- [15] R. Guo, Y. He, T. Yu, P. Cheng, J. You, H. Lin, C.-T. Chen, T. Chan, X. Liu, Z. Hu, Enhanced oxygen evolution reaction activity of flower-like FeOOH via the synergistic effect of sulfur, *Chem. Eng. J.* 420 (2021) 127587, <https://doi.org/10.1016/j.cej.2020.127587>.
- [16] J. Wang, J. Huang, S. Zhao, I.P. Parkin, Z. Tian, F. Lai, T. Liu, G. He, Mo/Fe bimetallic pyrophosphates derived from Prussian blue analogues for rapid electrocatalytic oxygen evolution, *Green. Energy Environ.* 8 (2023) 1450–1458, <https://doi.org/10.1016/j.gee.2022.02.014>.
- [17] Y. Wang, S. Chen, J. Zhang, Hierarchical assembly of prussian blue derivatives for superior oxygen evolution reaction, *Adv. Funct. Mater.* 29 (2019) 1904955, <https://doi.org/10.1002/adfm.201904955>.
- [18] H. Zhang, P. Li, S. Chen, F. Xie, D.J. Riley, Anodic transformation of a core-shell prussian blue analogue to a bifunctional electrocatalyst for water splitting, *Adv. Funct. Mater.* 31 (2021) 2106835, <https://doi.org/10.1002/adfm.202106835>.
- [19] F. Diao, M. Rykær Kraglund, H. Cao, X. Yan, P. Liu, C. Engelbrekt, X. Xiao, Moderate heat treatment of CoFe Prussian blue analogues for enhanced oxygen evolution reaction performance, *J. Energy Chem.* 78 (2023) 476–486, <https://doi.org/10.1016/j.jec.2022.11.050>.
- [20] C. Xuan, W. Lei, J. Wang, T. Zhao, C. Lai, Y. Zhu, Y. Sun, D. Wang, Sea urchin-like Ni-Fe sulfide architectures as efficient electrocatalysts for the oxygen evolution reaction, *J. Mater. Chem. A* 7 (2019) 12350–12357, <https://doi.org/10.1039/C9TA02761K>.
- [21] X. Ding, H. Huang, Q. Wan, X. Guan, Y. Fang, S. Lin, D. Chen, Z. Xie, Self-template synthesis of hollow Fe-doped CoP prisms with enhanced oxygen evolution reaction activity, *J. Energy Chem.* 62 (2021) 415–422, <https://doi.org/10.1016/j.jec.2021.04.001>.
- [22] V.T. Nguyen, F.N.I. Sari, B.W. Saputro, J.-M. Ting, Structural and defect modulations of co-precipitation synthesized high-entropy Prussian blue analogue nanocubes via Cu/Zn co-doping for enhanced electrochemical performance, *J. Mater. Chem. A* 11 (2023) 19483–19495, <https://doi.org/10.1039/D3TA01967E>.
- [23] X.-Y. Yu, Y. Feng, B. Guan, X.W. Lou, U. Paik, Carbon coated porous nickel phosphides nanoplates for highly efficient oxygen evolution reaction, *Energy Environ. Sci.* 9 (2016) 1246–1250, <https://doi.org/10.1039/C6EE00100A>.
- [24] Z. Chen, B. Fei, M. Hou, X. Yan, M. Chen, H. Qing, R. Wu, Ultrathin Prussian blue analogue nanosheet arrays with open bimetal centers for efficient overall water splitting, *Nano Energy* 68 (2020) 104371, <https://doi.org/10.1016/j.nanoen.2019.104371>.
- [25] Y. Guo, J. Tang, Z. Wang, Y. Sugahara, Y. Yamachi, Hollow porous heterometallic phosphide nanocubes for enhanced electrochemical water splitting, *Small* 14 (2018) e1802442, <https://doi.org/10.1002/smll.201802442>.
- [26] S. Huang, Q. Zhang, P. Xin, J. Zhang, Q. Chen, J. Fu, Z. Jin, Q. Wang, Z. Hu, Construction of Fe-doped NiS-NiS<sub>2</sub> heterostructured microspheres via etching prussian blue analogues for efficient water-urea splitting, *Small* 18 (2022) e2106841, <https://doi.org/10.1002/smll.202106841>.
- [27] M. Hou, S. Gong, L. Ji, J. Huang, M. Xu, Z. Chen, Three-dimensional porous ultrathin carbon networks reinforced PBAs-derived electrocatalysts for efficient oxygen evolution, *Chem. Eng. J.* 419 (2021) 129575, <https://doi.org/10.1016/j.cej.2021.1295750>.
- [28] S. Wang, J. Cai, C. Lv, C. Hu, H. Guan, J. Wang, Y. Shi, J. Song, A. Watanabe, X. Ge, General and scalable preparation of Prussian blue analogues on arbitrary conductive substrates and their derived metal phosphides as highly efficient and ultra-long-life bifunctional electrocatalysts for overall water splitting, *Chem. Eng. J.* 420 (2021) 129972, <https://doi.org/10.1016/j.cej.2021.129972>.
- [29] X. Lin, S. Cao, H. Chen, X. Chen, Z. Wang, S. Zhou, H. Xu, S. Liu, S. Wei, X. Lu, Boosting oxygen evolution reaction of hierarchical spongy NiFe-PBA/Ni<sub>3</sub>C(B) electrocatalyst: Interfacial engineering with matchable structure, *Chem. Eng. J.* 433 (2022) 133524, <https://doi.org/10.1016/j.cej.2021.133524>.
- [30] L. Qiu, Q. Wang, P. Yan, X.-Y. Yu, Chemical-physical synergistic etching enabling deep reconstruction of NiFe Prussian blue analogue for efficient oxygen evolution reaction and Zn-air batteries, *J. Mater. Chem. A* 10 (2022) 21251–21259, <https://doi.org/10.1039/D2TA06930J>.
- [31] W. Song, X. Teng, Y. Niu, S. Gong, X. He, Z. Chen, Self-template construction of hollow Fe-Co<sub>x</sub>P nanospheres for oxygen evolution reaction, *Chem. Eng. J.* 409 (2021) 128227, <https://doi.org/10.1016/j.cej.2020.128227>.
- [32] X.Y. Yu, L. Yu, H.B. Wu, X.W. Lou, Formation of nickel sulfide nanoframes from metal-organic frameworks with enhanced pseudocapacitive and electrocatalytic properties, *Angew. Chem. Int. Ed. Engl.* 54 (2015) 5331–5335, <https://doi.org/10.1002/anie.201500267>.
- [33] B.K. Kang, M.H. Woo, J. Lee, Y.H. Song, Z. Wang, Y. Guo, Y. Yamachi, J.H. Kim, B. Lim, D.H. Yoon, Mesoporous Ni-Fe oxide multi-composite hollow nanocages for efficient electrocatalytic water oxidation reactions, *J. Mater. Chem. A* 5 (2017) 4320–4324, <https://doi.org/10.1039/C6TA10094E>.
- [34] Y. Zhu, L. Zhang, X. Zhang, Z. Li, M. Zha, M. Li, G. Hu, Double functionalization strategy toward Co-Fe-P hollow nanocubes for highly efficient overall water

- splitting with ultra-low cell voltage, Chem. Eng. J. 405 (2021) 127002, <https://doi.org/10.1016/j.cej.2020.127002>.
- [35] S. Liu, S. Geng, L. Li, Y. Zhang, G. Ren, B. Huang, Z. Hu, J.F. Lee, Y.H. Lai, Y. H. Chu, Y. Xu, Q. Shao, X. Huang, A top-down strategy for amorphization of hydroxyl compounds for electrocatalytic oxygen evolution, Nat. Commun. 13 (2022) 1187, <https://doi.org/10.1038/s41467-022-28888-3>.
- [36] B. Wu, H. Qian, Z. Nie, Z. Luo, Z. Wu, P. Liu, H. He, J. Wu, S. Chen, F. Zhang, Ni<sub>3</sub>S<sub>2</sub> nanorods growing directly on Ni foam for all-solid-state asymmetric supercapacitor and efficient overall water splitting, J. Energy Chem. 46 (2020) 178–186, <https://doi.org/10.1016/j.jecchem.2019.11.011>.